Origin of the magic angle in twisted bilayer graphene from hybridization of valence and conduction bands

Guodong Yu,[1] Yunhua Wang,[2,3,*] Mikhail I. Katsnelson,[4] and Shengjun Yuan[3,4,†]

[1]*Center for Quantum Sciences and School of Physics, Northeast Normal University, Changchun 130024, China*

[2]*Lanzhou Center of Theoretical Physics & Key Laboratory for Quantum Theory and Applications of the Ministry of Education & Key Laboratory of Theoretical Physics of Gansu Province & School of Physical Science and Technology, Lanzhou University, Lanzhou 730000, China*

[3]*Key Laboratory of Artificial Micro- and Nano-structures of Ministry of Education and School of Physics and Technology, Wuhan University, Wuhan 430072, China*

[4]*Institute for Molecules and Materials, Radboud University, Heijendaalseweg 135, NL-6525 AJ Nijmegen, Netherlands*

(Received 19 April 2023; revised 2 July 2023; accepted 18 July 2023; published 26 July 2023)

The magic-angle phenomenon of twisted bilayer graphene (tBG), i.e, the nontrivial topological flat bands with vanishing Fermi velocity at half filling, has aroused prominent attention on superconductivity, correlated insulators, orbital magnetism, etc. Several efforts have been made to unravel the generation mechanism of the magic-angle phenomenon in tBG. Herein, we show that the hybridizations between the conduction band (CB) and valence band (VB) from different monolayers are critically responsible for the flat bands with band inversion as a signature of the magic-angle phenomenon. The proposed new mechanism for the magic-angle phenomenon is verified by the reversion of irreducible representations of energy bands at Γ point. We also discuss the effects of VB-VB and CB-CB hybridizations on the band structures of tBG. The tight-binding results indicate that the VB-VB and CB-CB hybridizations from different layers play the role of the moiré potential in real space and reduce the bandwidth in the framework of nearly-free electron model. Our conclusions can also give the explanation on the absence of the magic-angle phenomenon even with bandwidth reductions in twisted bilayer MoS_2 and BN.

DOI: 10.1103/PhysRevB.108.045138

I. INTRODUCTION

A twisted bilayer graphene (tBG) can be formed by overlaying one layer of graphene on top of another with a twist. Flat bands with vanishing Fermi velocity were predicted theoretically near neutrality in the tBG at a series of small twist angles, namely the magic angles [1]. Among them, only the largest magic angle ($\sim 1.05^\circ$) is stable and others disappear after the structural relaxation [2], and here we refer to the largest one once the magic angle is mentioned. The atomic relaxation changes the interlayer coupling strength and leads to shifts of the magic angle, but the narrow band phenomenon remains [3]. For materials with flat bands near the Fermi energy, the Coulomb interaction dominates over the kinetic energy because of the small group velocity, which puts the flat band materials into strongly correlated regime [4]. Over the past decade, the flat bands [5–7] and the novel strongly correlated physical phenomena of the magic-angle tBG, such as the magnetism [8–15], correlated insulator [16–26], superconductivity [16,27–36], linear-in-temperature resistivity [37–39], and intrinsic quantized anomalous Hall effect [40–42], have been widely studied in both theories and experiments.

Due to the importance of the flat bands, understanding the magic-angle phenomenon becomes one of the concerned tasks in condensed matter physics. Previous works have presented their explanations and understanding of the magic angle in tBG. Song *et al.* used winding number of Wilson loops and irreducible representations of high-symmetry **k** points to verify the flat band topology of tBG at magic angle [43]. Tarnopolsky *et al.* proposed a chirally symmetric continuum model for the emergence of flat bands and built a link between the flat bands and the lowest Landau level wave functions on torus [44]. Gao *et al.* claimed that the magic-angle phenomenon originates from the Heisenberg uncertainty principle [45].

In this paper, from the way of band hybridizations, we propose a new mechanism: the flat bands with band inversion as a signature of magic-angle phenomenon arise from the hybridizations between the conduction band (CB) and valence band (VB) from different monolayers. In the basis of CB and VB of the bottom and top monolayers, we discuss the effects of CB-CB, VB-VB, and VB-CB hybridizations from different layers on the band structures of tBG. We find that (i) the VB-VB and CB-CB hybridizations play the role of the moiré potential in real space and reduce the bandwidth in the way of nearly-free electron model (NFEM), and (ii) the VB-CB hybridization enables the band inversion and magic-angle flat bands in tBG. The symmetry analysis and the reversion of irreducible representations at Γ point for the band structures of tBG manifest the band inversion generated by the VB-CB

*wangyunhua@lzu.edu.cn
†s.yuan@whu.edu.cn

 ©2023 American Physical Society

hybridization from different layers near the magic angle. Our approach with an advantage of a more traditional language of band theory can be straightforwardly generalized to other two-dimensional (2D) materials including twisted bilayer MoS_2 and BN, and clarify the reason why the magic-angle phenomenon is absent even with the bandwidth reduction in these systems.

II. METHODS

Crystal structure.—Graphene has the hexagonal lattice with its lattice constant $a = 2.46$ Å and carbon-carbon bond length $b = 1.42$ Å. Here we choose $\boldsymbol{a}_1 = a(\frac{\sqrt{3}}{2}, -\frac{1}{2})$ and $\boldsymbol{a}_2 = a(\frac{\sqrt{3}}{2}, \frac{1}{2})$ as the lattice vectors of graphene, and choose $\boldsymbol{\tau}_A = b(1, 0)$ and $\boldsymbol{\tau}_B = b(2, 0)$ as the coordinates of two sublattices. Then the reciprocal lattice vectors are given by $\boldsymbol{b}_1 = \frac{2\pi}{a}(\frac{1}{\sqrt{3}}, -1)$ and $\boldsymbol{b}_2 = \frac{2\pi}{a}(\frac{1}{\sqrt{3}}, 1)$. Starting from the AA-stacked bilayer graphene with interlayer spacing fixed at 3.35 Å, we can obtain a tBG by rotating the top layer by an angle of θ anticlockwise with respect to the bottom layer. Then the lattice vectors and reciprocal lattice vectors of the top layer read $[R_\theta \boldsymbol{a}_1, R_\theta \boldsymbol{a}_2]$ and $[R_\theta \boldsymbol{b}_1, R_\theta \boldsymbol{b}_2]$, respectively, where R_θ is the rotation operation. The structure of a commensurate tBG can also be determined by two integers m and n uniquely. For a pair of m and n, the twist angle θ of the commensurate tBG satisfies

$$\cos\theta = \frac{m^2 + 4mn + n^2}{2(m^2 + mn + n^2)}, \tag{1}$$

and then these vectors correspondingly take the forms as

$$\begin{aligned} \boldsymbol{a}_1^m &= n\boldsymbol{a}_1 + m\boldsymbol{a}_2, \\ \boldsymbol{a}_2^m &= -m\boldsymbol{a}_1 + (m+n)\boldsymbol{a}_2, \end{aligned} \tag{2}$$

and

$$\begin{aligned} \boldsymbol{b}_1^m &= \frac{2\pi}{a}\frac{(m+n)\boldsymbol{i} + \frac{m-n}{\sqrt{3}}\boldsymbol{j}}{m^2+n^2+mn}, \\ \boldsymbol{b}_2^m &= \frac{2\pi}{a}\frac{-m\boldsymbol{i} + \frac{2n+m}{\sqrt{3}}\boldsymbol{j}}{m^2+n^2+mn}, \end{aligned} \tag{3}$$

respectively. In this paper, only the case of $m = n + 1$ is considered, because this choice always corresponds to the smallest number of atoms inside a unit cell at a given twist angle [46]. In addition, $m > n$ means the anticlosewise rotation of the top layer.

Tight-binding model.—The Hamiltonian of a tBG can be described by the p_z-orbital based tight-binding model as

$$H = \sum_i \varepsilon_0 c_i^\dagger c_i + \sum_{i\neq j} t(\boldsymbol{r}_{ij}) c_i^\dagger c_j, \tag{4}$$

where $c_i^\dagger$ and c_i are the creation and annihilation operators for p_z orbital at ith site, ε_0 is the onsite energy, and $t(\boldsymbol{r}_{ij})$ is the hopping energy between p_z orbitals at ith and jth sites with $\boldsymbol{r}_{ij}$ as their relative position vector. The Slater-Koster tight-binding hopping energy reads [47]

$$t(\boldsymbol{r}_{ij}) = n^2 V_{pp\sigma}(|\boldsymbol{r}_{ij}|) + (1-n^2)V_{pp\pi}(|\boldsymbol{r}_{ij}|), \tag{5}$$

where n is the direction cosine of $\boldsymbol{r}_{ij}$ with respect to the z axis, and the Slater-Koster parameters $V_{pp\sigma}$ and $V_{pp\pi}$ read

$$\begin{aligned} V_{pp\pi}(|\boldsymbol{r}|) &= -\gamma_0 e^{\delta(a_0 - |\boldsymbol{r}|)}, \\ V_{pp\sigma}(|\boldsymbol{r}|) &= \gamma_1 e^{\delta(h_0 - |\boldsymbol{r}|)}. \end{aligned} \tag{6}$$

We take the tight-binding parameters as $\varepsilon_0 = 0.0$ eV, $\gamma_0 = 2.8$ eV, $a_0 = 1.42$ Å, $\gamma_1 = 0.48$ eV, $h_0 = 3.35$ Å, and $\delta = 2.218$ Å^{-1}. The hoppings for carbon-carbon distance larger than 5 Å are ignored. This tight-binding model has been used in literatures and can reproduce the electronic structure in well accordance with experiments [48–52].

Low-energy model.—Based on the tight-binding model in real space given above, we introduce the low-energy model, which reproduces the accurate electronic structures of the tBG around the Fermi energy and needs relatively small computation resources. For a tBG, we define the Bloch functions of the two layers by

$$\begin{aligned} |\boldsymbol{k}_b, X_b\rangle &= \frac{1}{\sqrt{N}}\sum_{\boldsymbol{R}_{X_b}} e^{i\boldsymbol{k}_b\cdot\boldsymbol{R}_{X_b}} \left|\boldsymbol{R}_{X_b}\right\rangle \quad \text{(Bottom layer)}, \\ |\boldsymbol{k}_t, X_t\rangle &= \frac{1}{\sqrt{N}}\sum_{\boldsymbol{R}_{X_t}} e^{i\boldsymbol{k}_t\cdot\boldsymbol{R}_{X_t}} \left|\boldsymbol{R}_{X_t}\right\rangle \quad \text{(Top layer)}, \end{aligned} \tag{7}$$

where the bottom and top layers are labeled by the subscripts b and t, respectively, N is the normalization factor, $\boldsymbol{R}_{X_l}$ is the position of sublattice X_l (A or B) of layer l (b or t), and $|\boldsymbol{R}_{X_l}\rangle$ denotes the p_z orbital at position $\boldsymbol{R}_{X_l}$. Based on the Bloch functions, the Hamiltonian matrix has the form

$$H = \begin{bmatrix} H_b & U \\ U^\dagger & H_t \end{bmatrix}, \tag{8}$$

where H_b and H_t are the Hamiltonian matrices of the bottom and top layers, respectively, and U is the interlayer coupling matrix. The intralayer Hamiltonian matrix elements read

$$\begin{aligned} \langle \boldsymbol{k}_b, X_b|H_b|\boldsymbol{k}_b', X_b'\rangle &= h_{X_b X_b'}(\boldsymbol{k}_b)\delta_{\boldsymbol{k}_b,\boldsymbol{k}_b'}, \\ \langle \boldsymbol{k}_t, X_t|H_t|\boldsymbol{k}_t', X_t'\rangle &= h_{X_t X_t'}(\boldsymbol{k}_t)\delta_{\boldsymbol{k}_t,\boldsymbol{k}_t'}, \end{aligned} \tag{9}$$

and

$$\begin{aligned} h_{X_b X_b'}(\boldsymbol{k}_b) &= \sum_{\boldsymbol{L}_b} t(\boldsymbol{L}_b + \boldsymbol{\tau}_{X_b X_b'}) e^{i\boldsymbol{k}_b\cdot(\boldsymbol{L}_b + \boldsymbol{\tau}_{X_b X_b'})}, \\ h_{X_t X_t'}(\boldsymbol{k}_t) &= \sum_{\boldsymbol{L}_t} t(\boldsymbol{L}_t + \boldsymbol{\tau}_{X_t X_t'}) e^{i\boldsymbol{k}_t\cdot(\boldsymbol{L}_t + \boldsymbol{\tau}_{X_t X_t'})}, \end{aligned} \tag{10}$$

where the summation runs over all position vectors of the unit cell $\boldsymbol{L}_l$, and $\boldsymbol{\tau}_{X_l X_l'} = \boldsymbol{\tau}_{X_l'} - \boldsymbol{\tau}_{X_l}$ with $\boldsymbol{\tau}_{X_l}$ as the relative position of sublattice X_l inside a unit cell. The interlayer Hamiltonian matrix elements read [53–55]

$$\begin{aligned} &\langle \boldsymbol{k}_b, X_b|U|\boldsymbol{k}_t, X_t\rangle \\ &= \sum_{\boldsymbol{G}_b\boldsymbol{G}_t} T(\boldsymbol{k}_b + \boldsymbol{G}_b) e^{i\boldsymbol{G}_b\cdot\boldsymbol{\tau}_{X_b}} e^{-i\boldsymbol{G}_t\cdot\boldsymbol{\tau}_{X_t}} \delta_{\boldsymbol{k}_b+\boldsymbol{G}_b,\boldsymbol{k}_t+\boldsymbol{G}_t}, \end{aligned} \tag{11}$$

where $\boldsymbol{G}_b$ and $\boldsymbol{G}_t$ are the reciprocal points of the bottom and top layers, respectively, and $T(\boldsymbol{k}_b + \boldsymbol{G}_b)$ is the in-plane Fourier transform of the interlayer hopping function $t(\boldsymbol{r})$ at

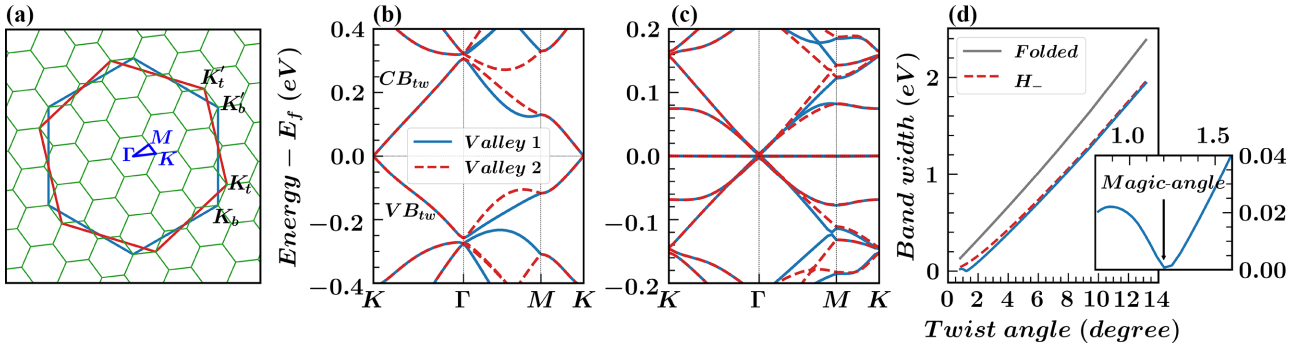

FIG. 1. (a) The Brillouin zones of 13.17°-tBG (green hexagonal networks) and two monolayers (blue and red hexagons). K_b and K_t (K_b' and K_t') are the K (K') valleys of the bottom and top layers. The band structures of 3.15°-tBG in (b) and 1.20°-tBG in (c). The bands of Valley 1 and Valley 2 originate from the couplings between two layers' K valleys and between two layers' K' valleys, respectively. The dependence of the bandwidth on the twist angle for VB_{tw} denoted by the solid blue line in (d) with the inset as its zoom-in near the magic angle, and the bandwidths of the highest H_- band (dashed red line) and the folded valence band closest to the Fermi energy of the decoupled bilayer (dashed gray line) are also plotted for comparison.

vector $\boldsymbol{k}_b + \boldsymbol{G}_b$, which is defined by

$$T(\boldsymbol{q}) = \frac{1}{S}\int t(\boldsymbol{r}_{xy} + h\hat{\boldsymbol{e}}_z)e^{-i\boldsymbol{q}\cdot\boldsymbol{r}_{xy}}d\boldsymbol{r}_{xy}, \tag{12}$$

where S is the area of the unit cell of graphene monolayer. For the tight-binding model we adopt that $T(\boldsymbol{q})$ only depends on the length of $\boldsymbol{q}$, namely $T(\boldsymbol{q}) = T(|\boldsymbol{q}|)$, and it decreases sharply with the growth of $|\boldsymbol{q}|$.

According to Eq. (11), the Bloch functions of the two layers can couple with each other if the reciprocal points $\boldsymbol{G}_b$ and $\boldsymbol{G}_t$ make the condition $\boldsymbol{k}_b + \boldsymbol{G}_b = \boldsymbol{k}_t + \boldsymbol{G}_t$ fulfilled. Therefore, we can define a lattice by the lattice vectors [56]

$$\begin{aligned}\boldsymbol{g}_1 &\equiv \boldsymbol{b}_1 - R_\theta\boldsymbol{b}_1 = (n-m)\left(\boldsymbol{b}_1^m + \boldsymbol{b}_2^m\right),\\ \boldsymbol{g}_2 &\equiv \boldsymbol{b}_2 - R_\theta\boldsymbol{b}_2 = (m-n)\boldsymbol{b}_1^m,\end{aligned} \tag{13}$$

which refer to the coupling lattice because $\boldsymbol{k}_b$ and $\boldsymbol{k}_t$ can couple with each other only if they are on the same coupling lattice, namely,

$$\begin{aligned}\boldsymbol{k}_b &= \boldsymbol{k}_0 + p_b\boldsymbol{g}_1 + q_b\boldsymbol{g}_2,\\ \boldsymbol{k}_t &= \boldsymbol{k}_0 + p_t\boldsymbol{g}_1 + q_t\boldsymbol{g}_2,\end{aligned} \tag{14}$$

with integers p_b, q_b, p_t, and q_t. These wavevectors in Eq. (14) construct a $\boldsymbol{k}_0$-dependent subspace, and the dimension of the $\boldsymbol{k}_0$-dependent subspace is infinitely large because there are not limitations of the integers p_b, q_b, p_t, and q_t. The interlayer coupling is much weaker than the intralayer interaction such that the electronic states of the tBG in the low-energy region almost originate from the coupling between the states of the two layers around the energy valleys. Therefore, we can limit $\boldsymbol{k}_b$ and $\boldsymbol{k}_t$ around the valley points to grasp the low-energy physics of the tBG.

III. RESULTS AND DISCUSSION

A. Review on the magic-angle phenomenon

We firstly present the magic-angle phenomenon in the tBG [1]. As shown in Figs. 1(b)–1(c), there are two valence bands (labeled by VB_{tw}) and two conduction bands (labeled by CB_{tw}) for tBG around the Fermi energy, and among these four bands one pair of valence and conduction subbands is from one energy valley, and the other pair is from the other energy valley. As we can see, the two VB_{tw} from different valleys have the same bandwidth, and so do the two CB_{tw}. In Fig. 1(d), the dependence of the bandwidths of the VB_{tw} on the twist angle θ shows clearly the magic-angle phenomenon of the tBG reported in literature [1]. That is, the bandwidth decreases when the twist angle decreases till the magic angle (θ_M) where the flat bands form with its bandwidth close to zero in Fig. 1(c), and then the bandwidth increases when the twist angle decreases further. Here our calculated magic angle is 1.20°, which slightly deviates from the other values of magic angle such as 0.99° [57], 1.05° [1], 1.08° [46], and 1.1° [27] in previous theories and experiments because of the adopted slightly different tight-binding parameters, while this has no influence on analyzing the emergence of magic-angle phenomenon in tBG. In addition, the relaxation does not ruin the formation of flat bands at the magic angle, even though the relaxation effect has influence on the detailed band structures [46], such as the band gap between the VB_{tw} and CB_{tw} bands and others.

B. Band inversion

To track the origins of the flat bands of the two VB_{tw} and two CB_{tw} of tBG at the magic angle, we project the states of the four bands on the eigenstates of the two decoupled monolayers and further define a $\boldsymbol{k}$-dependent function $\beta(\boldsymbol{k})$, which reflects how the conduction and valence bands of the decoupled monolayers contribute to a given eigenstate $|\varphi(\boldsymbol{k})\rangle$ of tBG, as

$$\beta(\boldsymbol{k}) = \sum_l |\langle\phi_{l,CB}(\boldsymbol{k})|\varphi(\boldsymbol{k})\rangle|^2 - \sum_l |\langle\phi_{l,VB}(\boldsymbol{k})|\varphi(\boldsymbol{k})\rangle|^2, \tag{15}$$

where $|\phi_{l,CB}(\boldsymbol{k})\rangle$ and $|\phi_{l,VB}(\boldsymbol{k})\rangle$ are the eigenstate states of conduction and valence bands of the layer l. We calculate $\beta(\boldsymbol{k})$ in Eq. (15) under different twist angles, as shown in Fig. 2. The results show that the valence (conduction) band states of the decoupled monolayers dominate the VB_{tw} (CB_{tw}) of the tBG for $\theta > \theta_M$. However, it is explicitly opposite for $\theta < \theta_M$. Therefore, the band inversion for tBG happens after

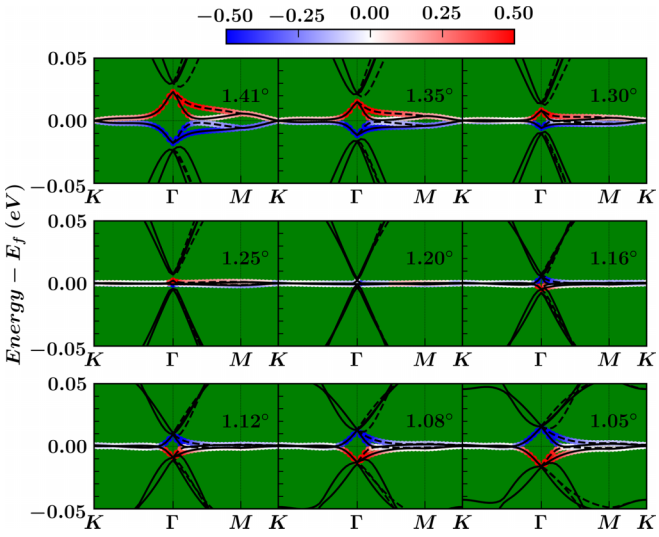

FIG. 2. The twist-angle-dependent evolution characteristics of the two VB_{tw} and two CB_{tw} of tBG from different valleys (solid and dashed lines) near the magic angle $\theta_M = 1.20°$. The color bar shows the $\beta(\boldsymbol{k})$ defined in Eq. (15).

the critical angle θ_M, i.e., the magic angle. Furthermore, the band inversion indicates that the bands of eigenstates from different layers are hybridized and then form the band structures of tBG, especially the flat bands.

C. Hybridizations between the conduction and valence bands from different monolayers

To see how the eigenstates of different monolayers interact leading to the band inversion phenomenon and the flat bands near the magic angle, we adopt the basis consisting of the valence band (VB) and conduction band (CB) eigenstates of the bottom and top monolayers to write the Hamiltonian as

$$H = \begin{pmatrix} H_- & \tilde{U} \\ \tilde{U}^\dagger & H_+ \end{pmatrix}, \tag{16}$$

where H_- and H_+ are the Hamiltonians for the VB and CB eigenstates of the bottom and top layers, respectively, with following forms

$$H_- = \begin{pmatrix} H_{b_-} & H_{b_-t_-} \\ H^\dagger_{b_-t_-} & H_{t_-} \end{pmatrix}, \quad H_+ = \begin{pmatrix} H_{b_+} & H_{b_+t_+} \\ H^\dagger_{b_+t_+} & H_{t_+} \end{pmatrix}, \tag{17}$$

and $\tilde{U}$ is the VB-CB hybridization

$$\tilde{U} = \begin{pmatrix} 0 & \tilde{U}_{b_-t_+} \\ \tilde{U}_{t_-b_+} & 0 \end{pmatrix}. \tag{18}$$

In Eq. (17), H_- contains H_{b_-} for the VB of the bottom layer, H_{t_-} for the VB of the top layer and the VB-VB hybridization $H_{b_-t_-}$ between the bottom and top layers, and similarly, H_+ contains corresponding H_{b_+}, H_{t_+}, and the CB-CB hybridization $H_{b_+t_+}$. In Eq. (18), $\tilde{U}_{b_-t_+}$ represents the hybridization between the VB of the bottom layer and the CB of the top layer, and similarly, $\tilde{U}_{b_+t_-}$ is the hybridization between the CB of the bottom layer and the VB of the top layer, but the VB-CB hybridizations for the same layer is zero because of the orthogonality between eigenstates. After the transformation of representations, we can find out the contributions of the valence and conduction bands of two layers on the band structures of tBG clearly. Moreover, we can study the effects of VB-VB, CB-CB, and VB-CB hybridizations separately.

Figure 3 shows the band structures of tBG given by Eq. (16) and the energy spectra of H_- and H_+ in Eq. (17) under several different twist angles. At the large twist angle of 9.43°, the energy spectrum of H_- and H_+ reproduce the band structure of tBG. This means that for large twist angles the VB-CB hybridization in Eq. (18) can be ignored. With the decreased twist angle such as 3.48°, the VB-CB hybridization has a little modification on energy spectra of H_- and H_+. However, when the twist angle is further reduced near the magic angle, namely, from 2.00° to 0.99° in Fig. 3, the energy spectra of H_- and H_+ are completely different from the band structures of tBG. This indicates that the VB-CB hybridization plays a critical role in the band structures of tBG, especially for the flat bands and the band inversion.

In Fig. 1(d), we have plotted the corresponding bandwidth for the folded band structure of graphene monolayer into the supercell of the tBG and the energy spectrum of H_- with the VB-VB and CB-CB hybridizations but without the VB-CB hybridization. The results indicate that the VB-VB and CB-CB hybridizations lead to the reduction of bandwidth through the whole range of twist angle. However, near the magic angle the appearance of the flat bands arise from the VB-CB hybridization, as shown in the inset of Fig. 1(d) and here in Fig. 3. Therefore, we can draw the conclusion that the VB-VB and CB-CB hybridizations only compress the bandwidth, but the VB-CB hybridization is actually responsible for the formation of flat bands with band inversion, i.e., the magic-angle phenomenon in Sec. III A. This conclusion also indicates that

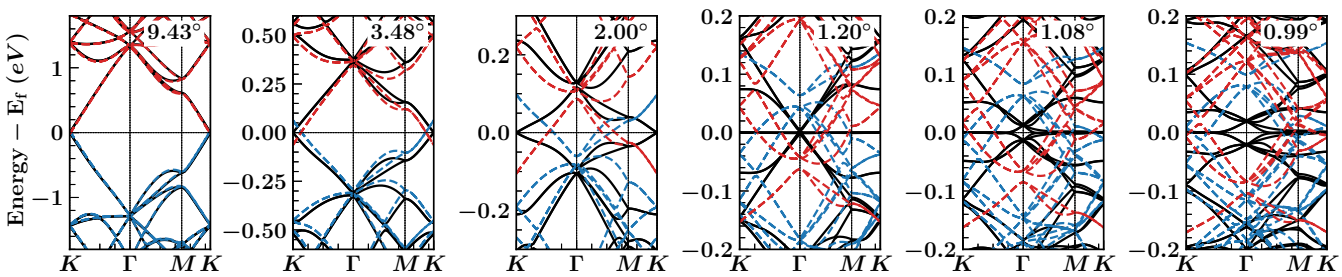

FIG. 3. The band structures of tBG (black lines), H_- (dashed blue lines), and H_+ (dashed red lines) under different twist angles varying from 9.43° to 0.99°, where the magic angle θ_M is at 1.2°.

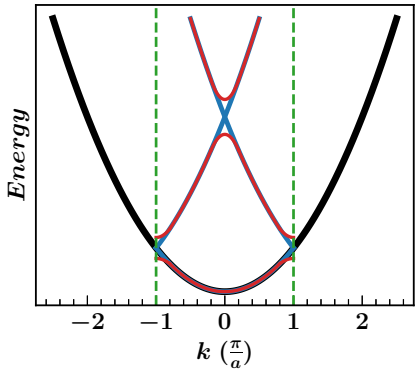

FIG. 4. The process of bandwidth reduction for free electrons modulated by the one-dimensional periodic potential $V(\boldsymbol{r})$ in NFEM. Here, the first Brillouin zone is denoted by $[-\pi/a, \pi/a]$ inside the two vertical green dashed lines with a as the periodicity of $V(\boldsymbol{r})$; the parabolic band of free electrons without potential is denoted by the black line with its folded bands into the Brillouin zone denoted by the blue lines; the isolated subbands with a finite bandwidth are denoted by the red lines due to the band gap opened by $V(\boldsymbol{r})$ at these crossing points $k = \pm\pi/a$ and $k = 0$.

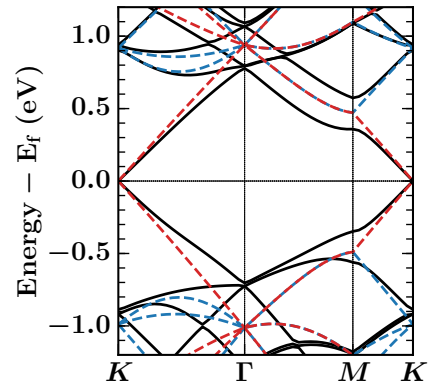

FIG. 5. The band structures of 6.01°-tBG (black lines) and its bottom layer (dashed blue lines) and top layer (dashed red lines).

the VB-CB hybridization is a new generated mechanism of band inversion beyond the spin-orbital coupling.

D. Nearly-free electron model for bandwidth reduction

We first review the nearly-free electron model (NFEM) and then explain that how the VB-VB and CB-CB hybridizations enable the bandwidth reduction rather than the formation of flat bands near the magic angle in the framework of NFEM.

Review on NFEM.—For a free electron with mass m, it has the parabolic dispersion $E(k) = \frac{\hbar^2 \boldsymbol{k}^2}{2m}$ and the plane-wave eigenfunctions $\varphi_{\boldsymbol{k}}(\boldsymbol{r}) = \langle \boldsymbol{r}|\boldsymbol{k}\rangle = \frac{1}{\sqrt{V}} e^{i\boldsymbol{k}\cdot\boldsymbol{r}}$ with the wavevector $\boldsymbol{k}$ and the sample volume V. There is only one band for the free electron with infinitely large bandwidth. We consider how the infinite bandwidth is compressed if a weak periodic potential $V(\boldsymbol{r})$ is applied with its periodicity $\boldsymbol{T} = \sum_i n_i \boldsymbol{a}_i$, where $\boldsymbol{a}_i$ is the lattice vector, n_i is any one integer, and the corresponding reciprocal lattice vectors $\boldsymbol{b}_j$ are given by $\boldsymbol{a}_i \cdot \boldsymbol{b}_j = 2\pi\delta_{ij}$ with the first Brillouin zone of $[-\pi/a, \pi/a]$ as shown in Fig. 4. After the Fourier transformation, the potential $V(\boldsymbol{r})$ is rewritten as $V(\boldsymbol{r}) = \sum_{\boldsymbol{G}} V_{\boldsymbol{G}} e^{-i\boldsymbol{G}\cdot\boldsymbol{r}}$, where $\boldsymbol{G} = \sum_i n_i \boldsymbol{b}_i$ runs over all the reciprocal points. In the plane-wave bases, the Hamiltonian matrix element takes the form as

$$\langle \boldsymbol{k}_1|H|\boldsymbol{k}_2\rangle = \frac{\hbar^2 \boldsymbol{k}_1^2}{2m}\delta_{\boldsymbol{k}_1\boldsymbol{k}_2} + \sum_{\boldsymbol{G}} V_{\boldsymbol{G}}\delta_{\boldsymbol{k}_2,\boldsymbol{k}_1+\boldsymbol{G}}, \tag{19}$$

where $H = H_0 + V(\boldsymbol{r})$ with the Hamiltonian H_0 of the free electron, $\boldsymbol{k}_1 = \boldsymbol{k} + \boldsymbol{G}_1$, and $\boldsymbol{k}_2 = \boldsymbol{k} + \boldsymbol{G}_2$ with $\boldsymbol{k}$ inside the first Brillouin zone. If $V(\boldsymbol{r})$ is zero, the original parabolic band of the free electron is folded into the small Brillouin zone of the periodic potential $V(\boldsymbol{r})$ and becomes a new set of subbands connected at the high-symmetry k points, as denoted by the blue lines in Fig. 4. However, the nonzero potential interaction in Eq. (19) gives the energy spectrum $E(\boldsymbol{k})$ with a gap opened at the crossing points of the subbands including $k = \pm\pi/a$ and $k = 0$, as denoted by red lines in Fig. 4. Consequently, the original energy band with an infinite bandwidth is compressed into several new bands with finite bandwidths [58].

NFEM for tBG.—We now turn to the bandwidth reduction enabled by the VB-VB and CB-CB hybridizations in tBG. As an example, we consider the tBG with a twist angle of 6.01° and plot both the folded bands (dashed blue or red lines) of graphene monolayers and the energy bands (solid black lines) of the tBG in Fig. 5. For a relatively large twist angle, the VB-CB hybridization is quite weak (see Sec. III C), and thus the interlayer hybridization is mainly from the VB-VB and CB-CB hybridizations between different monolayers. As seen from Fig. 5, the bandwidth for the energy bands of tBG is obviously narrower than those of graphene monolayers through the whole path from $K \to \Gamma \to M \to K$.

Furthermore, the bandwidth compression along the $\boldsymbol{k}$ path is nonuniform: (i) near K point, the large energy difference between the VB(CB) from top layer and the VB(CB) from the bottom layer induces relatively small VB-VB and CB-CB hybridizations, and thus the bandwidth compression is small; (ii) near Γ point, the small VB-VB and CB-CB energy differences between top and bottom layers lead to strong VB-VB and CB-CB hybridizations, and thus the bandwidth compression is remarkable.

In fact, for relatively large twist angles, the VB-VB and CB-CB hybridizations as the moiré potential in real space play the same role of potential hybridization in Eq. (19) for NEFM. Consequently, the VB-VB and CB-CB hybridizations enable the bandwidth reduction in the framework of NEFM. In addition, with the decreased twist angle, the first Brillouin zone of tBG decreases, and new subbands become the energy bands of tBG with more reduced bandwidth enabled by the VB-VB and CB-CB hybridizations, as shown in Fig. 1. However, near the magic angle, H_- and H_+ including the VB-VB and CB-CB hybridizations in spite of reducing the bandwidth can not produce the flat bands, where $\tilde{U}_{b_+t_-}$ representing the VB-CB hybridizations is responsible for the flat bands with band inversion, as discussed in Sec. III C.

IV. DISCUSSIONS

A. Twisted bilayer MoS_2 and BN

The bandwidth reduction has also been reported for twisted bilayer MoS_2 [59] and BN [60]. However, unlike tBG, there

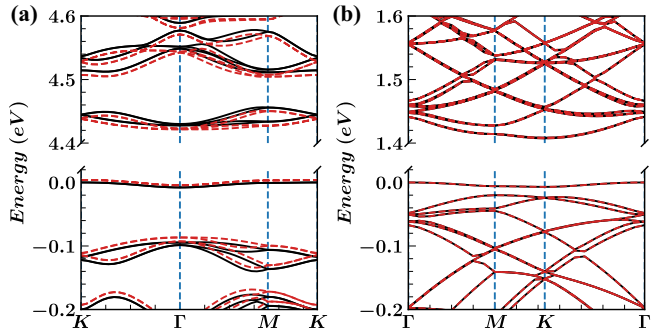

FIG. 6. The band structures (solid black lines) of (a) twisted bilayer BN with 3.15° and (b) twisted bilayer MoS_2 with 4.41°. The dashed red lines denote the band structures without the VB-CB hybridization. The adopted tight-binding parameters are taken from Ref. [61] and Ref. [62] for twisted bilayer BN and MoS_2, respectively.

is not the magic-angle phenomenon for their twisted bilayers. We have figured out that (i) the VB-VB and CB-CB hybridizations between different layers reduce the bandwidth, and (ii) the VB-CB hybridization is responsible for the magic-angle phenomenon. Actually our conclusions are also suitable for explaining the bandwidth reduction and the absence of magic-angle phenomenon in twisted bilayer MoS_2 and BN.

Different from graphene, both two-dimensional MoS_2 and BN are semiconductors with large band gaps. When stacking one layer of MoS_2 or BN on top of another, the VB-VB and CB-CB hybridizations always exist because of the same eigenenergy spectra of the two layers. Therefore, the bandwidth compression should be a common phenomenon in these twisted bilayers. However, for twisted bilayer MoS_2 and BN, the VB-CB hybridization between different layers is always quite weak even for a small twist angle because of the big energy difference from the wide band gap. In this way, the magic-angle phenomenon (i.e., the flat bands with band inversion) is absent for twisted bilayer MoS_2 and BN. In Fig. 6, we plot the band structure of twisted bilayer MoS_2 and BN with small twist angles and compare them with the energy spectra without the VB-CB hybridization. The numerical calculated results in Fig. 6 manifest our analysis.

B. Symmetry analysis on the band inversion

As presented in Sec. III B, the flat bands with the remarkable band inversion especially at Γ point is the signature of the magic-angle phenomenon. Here we use the irreducible representations (irreps) of the little group at Γ to examine the band inversion generated by the VB-CB hybridization near the magic angle θ_M. We adopt the following one-valley Moiré Hamiltonian [43,63] to describe the electronic energy states with corresponding symmetries:

$$H_{\boldsymbol{Q},\boldsymbol{Q}'}(\boldsymbol{k}) = \delta_{\boldsymbol{Q},\boldsymbol{Q}'} v_F(\boldsymbol{k}-\boldsymbol{Q})\cdot\boldsymbol{\sigma} + \omega\sum_{j=1}^{3}\left(\delta_{\boldsymbol{Q}-\boldsymbol{Q}',\boldsymbol{q}_j} + \delta_{\boldsymbol{Q}'-\boldsymbol{Q},\boldsymbol{q}_j}\right)T^j, \tag{20}$$

where $v_F = 10^6$ m/s is the Fermi velocity, w is the interlayer coupling strength, which is set to 0.135 eV agreeing with the energy values at $\theta_M = 1.2°$, and $T^j = \sigma_0 + \cos(\frac{2\pi}{3}j)\sigma_x + \sin(\frac{2\pi}{3}j)\sigma_y$ describes the way of the interlayer coupling among sublattices with the Pauli matrices (σ_x and σ_y) and the identity matrix σ_0. In Eq. (20), $\boldsymbol{q}_i$ with $i = 1, 2, 3$ connect the Brillouin zone corners of the two layers, and $\boldsymbol{Q}$ and $\boldsymbol{Q}'$ represent the wavevectors of the plane waves belonging to the bottom and top layers, respectively, as shown in Fig. 7. The Hamiltonian in Eq. (20) has the symmetry of magnetic space group $P6'2'2$ [43], and its generators are C_{3z} and C_{2x} with the representation matrix elements $D_{\boldsymbol{Q}',\boldsymbol{Q}}(C_{3z}) = e^{i\frac{2\pi}{3}\sigma_z}\delta_{\boldsymbol{Q}',C_{3z}\boldsymbol{Q}}$ and $D_{\boldsymbol{Q}',\boldsymbol{Q}}(C_{2x}) = \sigma_x\delta_{\boldsymbol{Q}',C_{2x}\boldsymbol{Q}}$. The character table of the little group at Γ point is given in Table I.

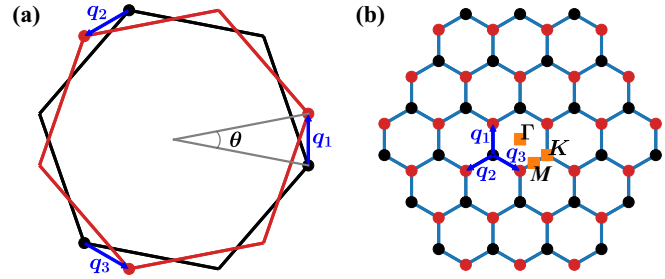

FIG. 7. (a) The Brillouin zones of two twisted graphene monolayers with three corners of the two layers connected by vectors $\boldsymbol{q}_i$ [43]. (b) The Brillouin zone of the tBG, where $\boldsymbol{Q}$ and $\boldsymbol{Q}'$ denoted by black and red dots are the wavevectors belonging to the bottom and top layers, respectively.

The irrep of a state at Γ point can be determined by the character projection operator P_{ir} by means of its property $P_{ir}\varphi_{ir'} = \delta_{ir,ir'}\varphi_{ir'}$, where $\varphi_{ir'}$ is a state having the irrep ir'. The character projection operator for the irrep ir is defined by $P_{ir} = \frac{l_{ir}}{g}\sum_R \chi^*_{ir}(R)D_R$ [55], where l_{ir} is the dimension of the irrep ir, $g = 6$ is the order of the group, $\chi_{ir}(R)$ is the character, and D_R is the representation matrix of the operation R for irrep ir. Actually, here we can also directly use the properties of the irreps and symmetry operators in Table I to judge the irrep of a state at Γ point for tBG. For instance, the two-fold degenerate energy levels must have the irrep Γ_3, and the states with eigenvalues of 1 and −1 for the operation C_{2x} have the irreps Γ_1 and Γ_2, respectively.

The calculated irreps at Γ point are labeled in Fig. 8. The irreps of VB_{tw} and CB_{tw} are correspondingly Γ_1 and Γ_2 at Γ point for $\theta > \theta_M$, and the irreps of VB_{tw} and CB_{tw} obviously take opposite irreps for $\theta < \theta_M$ compared with those for $\theta > \theta_M$. Therefore, the reversion of irreps at Γ point provides a direct proof for the band inversion. In addition, comparing the irreps of VB_{tw} and CB_{tw} with the irreps of the states for

TABLE I. The character table of irreps for the little group at Γ. E, C_3, and C_2' represent the conjugation classes generated from the identity, C_{3z}, and C_{2x}, respectively. The number before each conjugate class represents the number of operations in this class.

	Γ_1	Γ_2	Γ_3
E	1	1	2
$2C_3$	1	1	−1
$3C_2'$	1	−1	0

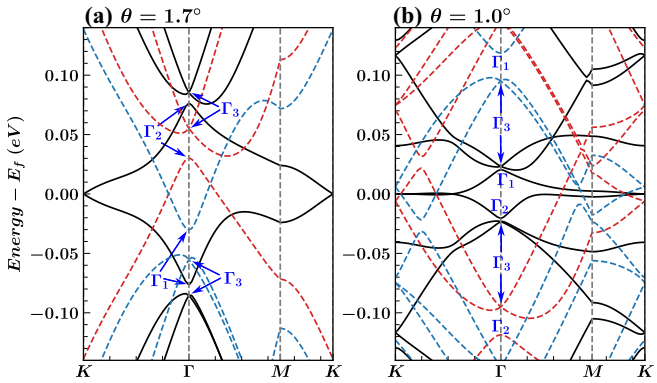

FIG. 8. The irreps of the VB_{tw} and CB_{tw} (solid black lines) at Γ for (a) 1.7°-tBG and (b) 1.0°-tBG using the Hamiltonian in Eq. (20). The blue and red dashed lines represent the energy bands of H_- and H_+, respectively. The irreps of the VB_{tw} (CB_{tw}) change from Γ_1 (Γ_2) to Γ_2 (Γ_1) with θ changing from 1.7° to 1.0°, and all twofold degenerate energy levels have the irrep Γ_3.

H_+ and H_-, we can also see how the CB-VB hybridization changes the bands of H_+ and H_- into the flat bands of tBG near the magnetic angle.

V. CONCLUSION

In summary, we proposed a new mechanism for magic-angle phenomenon in tBG, i.e., the flat bands with band inversion as a signature of magic-angle phenomenon is a result of the VB-CB hybridizations from different layers of tBG. Our tight-binding results show that the VB-VB and CB-CB hybridizations from different layers serve as the moiré potential in real space and enable the bandwidth reductions for any twist angle in the framework of NFEM. However, the VB-CB hybridization plays the critical role in the flat bands and the band inversion near the magic angle. The reversion of irreducible representations at Γ point provides a direct proof the band inversion induced by the VB-CB hybridization near the magic angle. Our conclusions on the VB-VB and CB-CB hybridizations reducing the bandwidth and the VB-CB hybridization enabling the flat bands and the band inversion are also suitable for explaining the absence of magic-angle phenomenon even with bandwidth reductions in twisted bilayer MoS_2 and BN.

ACKNOWLEDGMENTS

G.Y., S.Y., and Y.W. acknowledge support from the National Natural Science Foundation of China (Grants No. 12204092, No. 12174291, and No. 12247101). Y.W. acknowledges support from the 111 Project (Grant No. B20063) and the National Key Research and Development Program of China (Grant No. 2022YFA1402704). M.I.K. acknowledges the support by the ERC Synergy Grant, Project No. 854843 FASTCORR.

[1] R. Bistritzer and A. H. MacDonald, Proc. Natl. Acad. Sci. **108**, 12233 (2011).
[2] S. Carr, S. Fang, Z. Zhu, and E. Kaxiras, Phys. Rev. Res. **1**, 013001 (2019).
[3] F. Guinea and N. R. Walet, Phys. Rev. B **99**, 205134 (2019).
[4] L. Balents, C. R. Dean, D. K. Efetov, and A. F. Young, Nat. Phys. **16**, 725 (2020).
[5] M. I. B. Utama, R. J. Koch, K. Lee, N. Leconte, H. Li, S. Zhao, L. Jiang, J. Zhu, K. Watanabe, T. Taniguchi, P. D. Ashby, A. Weber-Bargioni, A. Zettl, C. Jozwiak, J. Jung, E. Rotenberg, A. Bostwick, and F. Wang, Nat. Phys. **17**, 184 (2021).
[6] S. Lisi, X. Lu, T. Benschop, T. A. de Jong, P. Stepanov, J. R. Duran, F. Margot, I. Cucchi, E. Cappelli, A. Hunter, A. Tamai, V. Kandyba, A. Giampietri, A. Barinov, J. Jobst, V. Stalman, M. Leeuwenhoek, K. Watanabe, T. Taniguchi, L. Rademaker *et al.*, Nat. Phys. **17**, 189 (2021).
[7] E. Suárez Morell, J. D. Correa, P. Vargas, M. Pacheco, and Z. Barticevic, Phys. Rev. B **82**, 121407(R) (2010).
[8] A. L. Sharpe, E. J. Fox, A. W. Barnard, J. Finney, K. Watanabe, T. Taniguchi, M. A. Kastner, and D. Goldhaber-Gordon, Science **365**, 605 (2019).
[9] S.-Y. Li, Y. Zhang, Y.-N. Ren, J. Liu, X. Dai, and L. He, Phys. Rev. B **102**, 121406(R) (2020).
[10] T. M. R. Wolf, J. L. Lado, G. Blatter, and O. Zilberberg, Phys. Rev. Lett. **123**, 096802 (2019).
[11] A. O. Sboychakov, A. V. Rozhkov, A. L. Rakhmanov, and F. Nori, Phys. Rev. Lett. **120**, 266402 (2018).
[12] L. A. Gonzalez-Arraga, J. L. Lado, F. Guinea, and P. San-Jose, Phys. Rev. Lett. **119**, 107201 (2017).
[13] R. Pons, A. Mielke, and T. Stauber, Phys. Rev. B **102**, 235101 (2020).
[14] L. Klebl, Z. A. H. Goodwin, A. A. Mostofi, D. M. Kennes, and J. Lischner, Phys. Rev. B **103**, 195127 (2021).
[15] J. Vahedi, R. Peters, A. Missaoui, A. Honecker, and G. T. de Laissardiére, SciPost Phys. **11**, 083 (2021).
[16] H. C. Po, L. Zou, A. Vishwanath, and T. Senthil, Phys. Rev. X **8**, 031089 (2018).
[17] N. F. Q. Yuan and L. Fu, Phys. Rev. B **98**, 045103 (2018).
[18] B. Padhi, C. Setty, and P. W. Phillips, Nano Lett. **18**, 6175 (2018).
[19] Y. Cao, V. Fatemi, A. Demir, S. Fang, S. L. Tomarken, J. Y. Luo, J. D. Sanchez-Yamagishi, K. Watanabe, T. Taniguchi, E. Kaxiras, R. C. Ashoori, and P. Jarillo-Herrero, Nature (London) **556**, 80 (2018).
[20] K. P. Nuckolls, M. Oh, D. Wong, B. Lian, K. Watanabe, T. Taniguchi, B. A. Bernevig, and A. Yazdani, Nature (London) **588**, 610 (2020).
[21] X. Liu, Z. Wang, K. Watanabe, T. Taniguchi, O. Vafek, and J. I. A. Li, Science **371**, 1261 (2021).
[22] Y. Zhang, K. Jiang, Z. Wang, and F. Zhang, Phys. Rev. B **102**, 035136 (2020).
[23] M. Ochi, M. Koshino, and K. Kuroki, Phys. Rev. B **98**, 081102(R) (2018).
[24] A. T. Pierce, Y. Xie, J. M. Park, E. Khalaf, S. H. Lee, Y. Cao, D. E. Parker, P. R. Forrester, S. Chen, K. Watanabe, T. Taniguchi, A. Vishwanath, P. Jarillo-Herrero, and A. Yacoby, Nat. Phys. **17**, 1210 (2021).

[25] Y. Da Liao, J. Kang, C. N. Breiø, X. Y. Xu, H.-Q. Wu, B. M. Andersen, R. M. Fernandes, and Z. Y. Meng, Phys. Rev. X **11**, 011014 (2021).
[26] M. Xie and A. H. MacDonald, Phys. Rev. Lett. **124**, 097601 (2020).
[27] Y. Cao, V. Fatemi, S. Fang, K. Watanabe, T. Taniguchi, E. Kaxiras, and P. Jarillo-Herrero, Nature (London) **556**, 43 (2018).
[28] H. Isobe, N. F. Q. Yuan, and L. Fu, Phys. Rev. X **8**, 041041 (2018).
[29] Y.-Z. Chou, Y.-P. Lin, S. Das Sarma, and R. M. Nandkishore, Phys. Rev. B **100**, 115128 (2019).
[30] G. Shavit, E. Berg, A. Stern, and Y. Oreg, Phys. Rev. Lett. **127**, 247703 (2021).
[31] E. Codecido, Q. Wang, R. Koester, S. Che, H. Tian, R. Lv, S. Tran, K. Watanabe, T. Taniguchi, F. Zhang, M. Bockrath, and C. N. Lau, Sci. Adv. **5**, eaaw9770 (2019).
[32] Y. Saito, J. Ge, K. Watanabe, T. Taniguchi, and A. F. Young, Nat. Phys. **16**, 926 (2020).
[33] M. Yankowitz, S. Chen, H. Polshyn, Y. Zhang, K. Watanabe, T. Taniguchi, D. Graf, A. F. Young, and C. R. Dean, Science **363**, 1059 (2019).
[34] F. Wu, A. H. MacDonald, and I. Martin, Phys. Rev. Lett. **121**, 257001 (2018).
[35] B. Lian, Z. Wang, and B. A. Bernevig, Phys. Rev. Lett. **122**, 257002 (2019).
[36] M. Oh, K. P. Nuckolls, D. Wong, R. L. Lee, X. Liu, K. Watanabe, T. Taniguchi, and A. Yazdani, Nature (London) **600**, 240 (2021).
[37] H. Polshyn, M. Yankowitz, S. Chen, Y. Zhang, K. Watanabe, T. Taniguchi, C. R. Dean, and A. F. Young, Nat. Phys. **15**, 1011 (2019).
[38] Y. Cao, D. Chowdhury, D. Rodan-Legrain, O. Rubies-Bigorda, K. Watanabe, T. Taniguchi, T. Senthil, and P. Jarillo-Herrero, Phys. Rev. Lett. **124**, 076801 (2020).
[39] F. Wu, E. Hwang, and S. Das Sarma, Phys. Rev. B **99**, 165112 (2019).
[40] M. Serlin, C. L. Tschirhart, H. Polshyn, Y. Zhang, J. Zhu, K. Watanabe, T. Taniguchi, L. Balents, and A. F. Young, Science **367**, 900 (2020).
[41] N. Bultinck, S. Chatterjee, and M. P. Zaletel, Phys. Rev. Lett. **124**, 166601 (2020).
[42] J. Liu and X. Dai, Phys. Rev. B **103**, 035427 (2021).
[43] Z. Song, Z. Wang, W. Shi, G. Li, C. Fang, and B. A. Bernevig, Phys. Rev. Lett. **123**, 036401 (2019).
[44] G. Tarnopolsky, A. J. Kruchkov, and A. Vishwanath, Phys. Rev. Lett. **122**, 106405 (2019).
[45] Y. Gao and X. Zhu, J. Phys. Chem. Lett. **12**, 9124 (2021).
[46] N. Leconte, S. Javvaji, J. An, A. Samudrala, and J. Jung, Phys. Rev. B **106**, 115410 (2022).
[47] J. C. Slater and G. F. Koster, Phys. Rev. **94**, 1498 (1954).
[48] G. Trambly de Laissardière, D. Mayou, and L. Magaud, Phys. Rev. B **86**, 125413 (2012).
[49] G. Trambly de Laissardière, D. Mayou, and L. Magaud, Nano Lett. **10**, 804 (2010).
[50] G. Yu, Z. Wu, Z. Zhan, M. I. Katsnelson, and S. Yuan, npj Comput. Mater. **5**, 122 (2019).
[51] G. Yu, Z. Wu, Z. Zhan, M. I. Katsnelson, and S. Yuan, Phys. Rev. B **102**, 115123 (2020).
[52] Y. Wang, G. Yu, M. Rösner, M. I. Katsnelson, H.-Q. Lin, and S. Yuan, Phys. Rev. X **12**, 021055 (2022).
[53] M. Koshino, New J. Phys. **17**, 015014 (2015).
[54] M. Koshino and P. Moon, J. Phys. Soc. Jpn. **84**, 121001 (2015).
[55] G. Yu, Y. Wang, M. I. Katsnelson, H.-Q. Lin, and S. Yuan, Phys. Rev. B **105**, 125403 (2022).
[56] D. Weckbecker, S. Shallcross, M. Fleischmann, N. Ray, S. Sharma, and O. Pankratov, Phys. Rev. B **93**, 035452 (2016).
[57] S. Pathak, T. Rakib, R. Hou, A. Nevidomskyy, E. Ertekin, H. T. Johnson, and L. K. Wagner, Phys. Rev. B **105**, 115141 (2022).
[58] S. V. Vonsovsky and M. I. Katsnelson, *Quantum Solid-State Physics* (Springer-Verlag, Berlin, Heidelberg, New York, 1989).
[59] Z. Zhan, Y. Zhang, P. Lv, H. Zhong, G. Yu, F. Guinea, J. A. Silva-Guillén, and S. Yuan, Phys. Rev. B **102**, 241106(R) (2020).
[60] X.-J. Zhao, Y. Yang, D.-B. Zhang, and S.-H. Wei, Phys. Rev. Lett. **124**, 086401 (2020).
[61] M. Long, P. A. Pantaleón, Z. Zhan, F. Guinea, J. Á. Silva-Guillén, and S. Yuan, npj Comput. Mater. **8**, 73 (2022).
[62] S. Fang, R. Kuate Defo, S. N. Shirodkar, S. Lieu, G. A. Tritsaris, and E. Kaxiras, Phys. Rev. B **92**, 205108 (2015).
[63] Z.-D. Song, B. Lian, N. Regnault, and B. A. Bernevig, Phys. Rev. B **103**, 205412 (2021).